OMI NO_2 column densities over North American urban cities: The effect of satellite footprint resolution

Hyun Cheol Kim[1,2], Pius Lee[1], Laura Judd[3], Li Pan[1,2], and Barry Lefer[3]

[1] NOAA/Air Resources Laboratory, College Park, MD

[2] UMD/Cooperative Institute for Climate and Satellites, College Park, MD

[3] University of Houston, Houston, TX

Abstract

Nitrogen dioxide vertical column density (NO_2 VCD) measurements via satellite are compared with a fine-scale regional chemistry transport model, using a new approach that considers varying satellite footprint sizes. Space-borne NO_2 VCD measurement has been used as a proxy for surface nitrogen oxide (NO_x) emission, especially for anthropogenic urban emission, so accurate comparison of satellite and modeled NO_2 VCD is important in determining the future direction of NO_x emission policy. The National Aeronautics and Space Administration Ozone Monitoring Instrument (OMI) NO_2 VCD measurements, retrieved by the Royal Netherlands Meteorological Institute (KNMI), are compared with a 12-km Community Multi-scale Air Quality (CMAQ) simulation from the National Oceanic and Atmospheric Administration. We found that OMI footprint pixel sizes are too coarse to resolve urban NO_2 plumes, resulting in a possible underestimation in the urban core and overestimation outside. In order to quantify this effect of resolution geometry, we have made two estimates. First, we constructed pseudo-OMI data using fine-scale outputs of the model simulation. Assuming the fine-scale model output is a true measurement, we then collected real OMI footprint coverages and performed conservative spatial regridding to generate a set of fake OMI pixels out of fine-scale model outputs. When compared to the original data, the pseudo-OMI data clearly showed smoothed signals over urban locations, resulting in roughly 20–30 % underestimation over major cities. Second, we further conducted conservative downscaling of OMI NO_2 VCD using spatial information from the fine-scale model to adjust the spatial distribution, and also applied Averaging Kernel (AK) information to adjust the vertical structure. Four-way comparisons were conducted between OMI with and without downscaling and CMAQ with and without AK information. Results show that OMI and CMAQ NO_2 VCDs show the best agreement when both downscaling and AK methods are applied, with correlation coefficient R = 0.89. This study suggests that satellite footprint sizes might have a considerable effect on the measurement of fine-scale urban NO_2 plumes. The impact of satellite footprint resolution should be considered when using satellite observations in emission policy making, and the new downscaling approach can provide a reference uncertainty for the use of satellite NO_2 measurements over most cities.

1. Introduction

Tropospheric nitrogen dioxide, NO_2, is an important component of urban atmospheric chemistry. It is one of the major pollutants affecting humans and the biosphere (Chauhan et al., 2003; Kampa and Castanas, 2008), and works as an important precursor in tropospheric ozone chemistry and aerosol formation. Continuous monitoring of tropospheric NO_2 is important to understand urban air quality and changes in anthropogenic emissions. NO_2 is also used as an important indicator for traffic and urbanization (Rijnders et al., 2001; Ross et al., 2006; Studinicka et al., 1997).

Tropospheric NO_2 has been measured from space since the mid-1990s; the Global Ozone Monitoring Experiment (GOME, 1996–2003, onboard the European Remote Sensing-2), Scanning Imaging Absorption SpectroMeter for Atmospheric CHartographY (SCIAMACHY, 2002–2012, onboard ENVISAT), Ozone Monitoring Instrument (OMI, 2004–present, onboard Aura), and GOME-2 (2007–present, onboard MetOp-A and 2013–present on MetOp-B) have all been used for the detection of NOx emission from natural and anthropogenic sources (Beirle et al., 2004; Boersma et al., 2007; Kim et al., 2006, 2009; Konovalov et al., 2006; Lamsal et al., 2008; Martin et al., 2003; Napelenok et al., 2008; Richter et al., 2005; van der A et al., 2006, 2008)

NO_2 plumes from urban anthropogenic sources, especially from point and mobile sources, usually have a fine structure, as small as a few hundred meters and as large as 10–20 km, as reported in comparisons of column NO_2 based on in situ observations and modeled calculations (Heue et al., 2008; Valin et al., 2011; Ryerson et al., 2001). Heue et al., (2008) used an airborne instrument based on imaging Differential Optical Absorption Spectroscopy (iDOAS) to build a two-dimensional distribution model of urban plumes. By comparing NO_2 column densities over the industrialized South African Highveld with OMI and SCIAMACHY measurements, they demonstrated that iDOAS shows strong enhancements close to industrial areas, 4–9 times higher than measurements from OMI and SCIAMACHY. Previous studies have demonstrated that modeled ozone production depends strongly on the spatial scale of the modeling grid due to the nonlinear dependence of ozone production on NOx concentration (e.g., Cohan et al., 2006; Gillani and Pleim, 1996; Liang and Jacobson, 2000; Sillman et al., 1990), so an accurate comparison of urban NO_2 plumes in fine scale is crucial for understanding surface ozone chemistry and air pollution over urban cities. Using 1-D and 2-D models, Valin et al., (2011) computed the resolution-dependent bias in the predicted NO_2 column, demonstrating large negative biases over large sources and positive biases over small sources at coarse model resolution.

The inhomogeneity of urban NO_2 plumes within the scale of satellite footprint pixels is of rising interest as satellite-based measurements are being compared with fine-scale modeling (Beirle et al., 2004; Beirle et al., 2011; Hilboll et al., 2013). Richter et al. (2005) showed that there are considerable differences between GOME and SCIAMACHY observations for locations with steep gradients in the tropospheric NO_2 columns, while these observations agree very well over large areas of relatively homogeneous NO_2 signals. Hilboll et al. (2013) argued that these effects result from spatial smoothing that differs depending on the ground resolution of the instruments, so the inherent spatial heterogeneity of the NO_x fields must be considered when studying them over small, localized areas. Hilboll et al. (2013) also presented approaches to account for instrumental differences while preserving individual instruments' spatial resolutions. In comparing GOME and SCIAMACHY, they used an explicit climatological correction factor to convolve GOME pixels (40×320 km^2) with better-resolution SCIAMACHY (30×60 km^2) data, producing a combined data set for studying long-term trends.

In this study, we try to investigate and to quantify the uncertainty resulting from the geometry of OMI satellite-based NO_2 VCD measurements by comparing these data to a fine-scale regional quality model. First, a pseudo-OMI data set is built from the outputs of fine-scale model simulations, and then these results are compared to model data in order to quantify the impact from pure differences in geometry. Second, we extend the basic concept of Hilboll et al. (2013) to apply spatial-distribution information from the fine-scale model to the OMI measurements, and demonstrate how the new approach adjusts the original OMI measurements. Satellite and model data are described in Section 2. Construction of pseudo-OMI data and the quantification of the impact of pixel geometry are discussed in Section 3. In Section 4, the downscaling approach is discussed; Section 5 concludes and discusses the implications of findings for emission policy decision-making.

2. Data

OMI: We utilized OMI tropospheric NO_2 VCD data, retrieved by the Royal Netherlands Meteorological Institute (KNMI). The OMI instrument, onboard NASA's Earth Observing System Aura satellite, is a nadir-viewing imaging spectrograph measuring backscattered solar radiation with a measuring wavelength ranging from 270 to 500 nm and with a spectral resolution of about 0.5 nm. Its telescope has a 114° viewing angle, which corresponds to a 2600 km-wide swath on the surface. In its normal global operation mode, its pixel size is 13 km (along) × 24 km (across) at nadir, which can be reduced to 13 km × 12 km in zoom mode (Levelt et al., 2006). Data were downloaded from the European Space Agency's (ESA) Tropospheric Emission Monitoring Internet Service (TEMIS; http://www.temis.nl/airpollution/no2.html). DOMINO version 2.0 retrieval based on the Differential Optical Absorption Spectroscopy (DOAS) technique was used for the study. We disregarded data pixels with cloud fractions over 40% or other contaminated pixels using quality flags. Details on the NO_2 column retrieval algorithms and error analysis are described in Boersma et al. (2004, 2007).

NAQFC: The U.S. National Air Quality Forecast Capability (NAQFC) provides daily, ground-level ozone predictions using the Weather Forecasting and Research non-hydrostatic mesoscale model (WRF-NMM) and CMAQ framework across the CONUS with a 12-km resolution domain (Chai et al., 2013; Eder et al., 2009). In our analysis, we used the experimental version of NAQFC, which uses WRF-NMM with B-grid (NMMB) as a meteorological driver and the CB05 chemical mechanism. Meteorological data is processed using the PREMAQ, which is a special version of the Meteorology-Chemistry Interface Processor (MCIP) designed for the NAQFC system. Emissions are projected to 2012 level using Department of Energy Annual Energy Outlook and EPA Cross-State Air Pollution Rule (CSAPR) from the 2005 National Emission Inventory. Detailed information on the emission is available from Pan et al., (2014) and references within.

3. Construction of pseudo-OMI data

OMI footprint pixel size increases as the viewing angle deviates from the nadir direction to the edge of swaths. Figure 1 shows the actual size distributions of OMI pixels collected during September 2013. The blue line indicates size distribution counts for each 50 km^2 bin, while the red line indicates the cumulative distribution of the OMI pixel sizes. The size distribution has high occurrences near 300 km^2, as expected from the OMI's resolution at the nadir (that is, 13x24 = 312). However, many pixels still have larger sizes; around half of total pixels are larger than 500 km^2, and 20% of total pixels are larger even than 1000 km^2. Geographical coverage rapidly increases with pixel size, so deciding a threshold for footprint pixel sizes and available coverage may present a serious dilemma.

Figure 2 shows the relationship between OMI footprint pixel size and actual geographical coverage over the Contiguous United States (CONUS). With 1 July 2011 data, 25% of OMI pixel sizes are less than 342 km^2, and they cover 1.4% of the CONUS domain. CONUS coverage changes to 11.5%, 24.0%, and 58.8% when 50%, 75%, and 100% of OMI pixels are used, respectively. Using only finer data may provide detailed information, but they represent only a small part of all the data. If we also use coarser-resolution data, they provide more coverage but tend to be biased over areas with spatial gradient, as discussed in the previously mentioned studies (Hilboll et al., 2013). We therefore estimated the theoretical range of biases deriving from this geometric effect by constructing a pseudo-OMI data set out of a fine-scale model. Using the fine-scale regional CMAQ simulations and assuming this model represents a true world, we constructed a dataset to mimic OMI instrument measurement of this modeled world.

In order to construct the pseudo-OMI data, we utilized a conservative spatial regridding technique to perform a lossless conversion of gridded modeling outputs into actual OMI footprint pixels. Figure 3 demonstrates the concepts of conservative regridding. The gray grid cells are 12-km grid cells for modeling—zoomed on the Houston region as an example—and the blue lines are actual OMI pixel coverage. The blue, shaped pixel is an example of an actual OMI pixel, while the pink boxes are model grid cells overlaid by the example OMI pixel. The numbers in the grid cells are calculations of the fractional area overlaid by the OMI pixel for each cell using the Sutherland-Hodman polygon-clipping algorithms available from the IDL-based Geospatial Data Processor (Kim et al., 2013); 0.74 means the OMI pixel covers 74% of the corresponding grid cell. The pseudo-OMI value for the blue OMI pixel area in Figure 3 can be estimated as:

$$P_j = \frac{\sum(p_i \cdot f_{i,j})}{\sum f_{i,j}} \tag{1}$$

where *i* and *j* are indices for the model grid cell and OMI pixel, respectively. $f_{i,j}$ indicates the fractional area of cell *i* overlaid by OMI pixel *j*.

Figure 4 compares the spatial distributions of CMAQ NO_2 VCD (assumed to be a true world) and pseudo-OMI (pOMI) NO_2 VCD, along with the difference and percentage difference, (pOMI-CMAQ)/CMAQ x 100, over the northeastern United States. It is evident that there are prominent differences between the original fine-scale modeled NO_2 VCD and reconstructed pseudo-OMI distribution, especially over and near urban locations. As expected from the smoothing effects of larger pixel sizes, pOMI shows a slightly smoothed transition from urban cores to suburban, and most of the sharp peaks near small cities are gone in the pOMI distribution. As already mentioned, this is purely a result of geometry. We can see that, for all the major cities, pOMI underestimates the actual NO_2 VCD values while overestimating at the boundaries of major cities, as clearly seen in the New York, Pittsburgh, Philadelphia, Baltimore, and Washington D.C. areas. This effect is also prominent in locations with small but strong NOx emission sources, such as power plants or small cities such as Norfolk, VA. It should be noted that these discrepancies result from purely geometric effects deriving from OMI's designed pixel sizes and are around +- 5–10x 10^15 #/cm2, with 20–30 % underestimation or overestimation biases for major cities and more than 100% under- or overestimation for local cities like Norfolk and Richmond, VA. In the next section, we introduce a new approach—the conservative downscaling method—to reduce this effect of resolution due to varying OMI footprint pixel sizes.

4. OMI NO_2 VCD downscaling

As described in the previous section, urban NO_2 plumes usually have too fine of a spatial structure compared to OMI's measuring footprints. In this section, we introduce a new approach for adjusting those geometric effects. Downscaling is a common concept in meteorological simulations, used especially in global circulation models to provide initial and boundary conditions for regional models. We use a similar concept, describing a downscaling method in data processing as a special case of spatial regridding that provides further details through the incorporation of additional information into a set of coarse-resolution data. This approach differs from simply increasing the resolution, as the raw, coarse data are restructured using a set of logics, analogous to a regional meteorological model that downscales global meteorology using its own set of physical and thermal field balances. Conceptually, we use a calculation process reversed from that used to construct the pseudo-OMI data set.

Figure 5 graphically depicts the steps of conservative downscaling from OMI pixels. Figure 5a shows actual OMI NO_2 VCD measurements over Los Angeles on May 4, 2010, and Figure 5b shows the corresponding CMAQ NO_2 VCD calculated from NAQFC modeling outputs at the same time and location. As readers can easily see, OMI footprint pixels are much bigger (~650 km^2) than are CMAQ grid cells (12x12 = 144 km^2). As a result, an OMI pixel can overlay more than 10 CMAQ grid cells, as demonstrated in Figure 5b (black box representing the OMI pixel). We collected those CMAQ pixel values and then normalized them so that the total value of each grid cell sums to one. We call this a spatial-weighting kernel (Figure 5c), and we apply this weighting kernel to the original OMI measurement. As a result, we generate a reconstructed OMI pixel with finer structure but without any loss of original quantity. Summing the reconstructed pixels gives the original OMI pixel measurement. It should be noted that we strictly apply this method conservatively; theoretically, if there are no missing or duplicated pixels, the quantity of the original data is numerically preserved. This method can be summarized as fusing a satellite-measured "quantity" with modeled "spatial information"; the strength of the modeled NO_2 field does not at all affect the result.

As expected, the accuracy of this method indeed depends on the model's performance, especially regarding its wind-field simulation and inputs of emission source locations, so this method clearly has its own limitation. Considering the uncertainties resulting from emission source locations, the air-quality community has had an excellent archive of geographical information about the geophysical locations of emission sources thanks to the efforts of U.S. EPA, although the strengths of these sources are somewhat highly uncertain. As just described, however, the downscaling method is not affected by emission strength, so we do not think that the uncertainty associated with known emission source is very high. On the other hand, the use of downscaling method can be limited when there are uncertainties in emission inventory information such as unknown emission sources or removal or known sources. Wind field is important for simulating NO_2 plume transport. With the short lifetime of NO_2, especially during summer, the spatial distribution of NO_2 plumes is strongly determined by the location of emission sources. Improving information about emission-source locations would somewhat improve the model, but it is more important to note that the downscaling method tends to convert the error characteristics. Near urban cores, OMI's coarse footprint resolution always causes unidirectional, systematic biases, with underestimation near urban cores and overestimation at the urban boundary. Using the downscaling method, these systematic biases from resolution are converted to random bias from wind-field error. Since these biases are random, they may be corrected by averaging over a certain time period, unlike the systematic bias resulting from resolution.

4.1. 2010 CalNex campaign case

We applied the downscaling technique to compare OMI and downscaled OMI with aircraft-borne measurements from the California Research at the Nexus of Air Quality and Climate (CalNex) campaign. The CalNex field study was conducted in California from May to July 2010 and focused on atmospheric-pollution and climate-change issues, including an emission inventory, atmospheric transport and dispersion, atmospheric chemical processing, cloud-aerosol interaction, and aerosol radiative effects (Ryerson et al., 2013). Here, we compared NO_2 VCD observations from the campaign's P3 flight with corresponding OMI measurements using both the standard and downscaling methods. More detailed descriptions regarding data preparation and a discussion of the influence of environmental inhomogeneity and urban NO2 plumes are provided by Judd et al. (2015)

Figure 6 shows scatter-plot comparisons between the P3 measurements and OMI NASA standard product (Figure 6a), OMI KNMI product (Figure 6b), and OMI KNMI downscaled (Figure 6c) for three days: 4, 7, and 16 May 2010. As reported, the OMI NO_2 VCD tends to underestimate near the Los Angeles urban area. The KNMI retrieval showed a slightly better comparison with slope = 0.73 and R = 0.85, while the downscaled product clearly showed the best agreement with the P3 measurements, R = 0.88 and slope = 1.0. Deviations still remain from a true one-to-one line even with the downscaling method; these are possibly caused by errors in wind field simulation. We expect these random errors to average out as the amount of available data increases. The downscaling method seems to work even with daily time-scale data sets.

Figure 7 compares OMI NO_2 VCD spatial distributions for the original KNMI products with downscaled products for 4 May 2010, the day when the downscaling method gave the most dramatic changes in the spatial distribution. In the original retrieval, OMI pixels were coarse and mostly smoothed out over Los Angeles. However, by applying the downscaling technique, the adjusted OMI data show a shape much closer to the urban boundary and enhanced NO_2 VCD values at the center of Los Angeles, agreeing very well with the P3 aircraft measurements. On 7 May, the downscaling method reproduced several peak values very well but failed to generate a clean spot at the edge of Los Angeles. On 16 May, the changes from downscaling are not dramatic due to generally low NO_2 concentrations due to less urban traffic on Sunday (e.g. the weekend effect), but the downscaling method still showed slight enhancement (shown in supplementary plots).

4.2. Comparison with NAQFC

Comparing modeled NO_2 VCD to satellite-observed NO_2 VCD has been a popular way to evaluate the NO_x emission inventory. Since modeled NO_2 VCD and satellite NO_2 VCD have different optical and vertical properties, some researchers have used additional processing to fairly compare satellite and modeled column densities. In this section, we performed vertical and spatial adjustment by applying Averaging Kernel (AK) information in conjunction with the downscaling technique. First, we compared NAQFC NO_2 VCD with and without AK to OMI NO_2 VCD with and without downscaling processing.

The sensitivity of the instrument to tropospheric tracer density is highly height-dependent. Since the measured tracer profile may have large systematic errors as a result, the retrieved tracer columns should be interpreted with proper additional information (Eskes and Boersma, 2003). An AK stores an instrument's relative sensitivity to the abundance of the target species for each layer throughout the atmospheric column (Bucsela et al., 2008) and can be applied to a modeled atmospheric column for a fair comparison with satellite retrievals. For each OMI DOMINO product pixel, 34 layers of AKs are provided. We first converted total AK to tropospheric AK, AK_{trop}, by applying the total air mass factor (AMF) and tropospheric AMF, and we then applied AK_{trop} to model layers before vertically integrating, as described by Herron-Thorpe et al. (2010). When multiple OMI pixels overlaid a model grid cell, we conducted the conservative spatial remapping method explained above.

Figure 8 compares the monthly averaged NO_2 VCD distributions for CMAQ without and with AK (Figure 8a & Figure 8b, respectively) and for OMI NO_2 VCD without and with downscaling (Figures 8c & 8d, respectively). In general, AK-applied CMAQ NO_2 VCD tends to be slightly lower than CMAQ NO_2 VCD without AK information. On the other hand, while OMI NO_2 VCD without DS shows a much smoother pattern, the DS-applied OMI reconstructs the sharp spatial structures near urban areas. DS-applied OMI NO_2 VCD is evidently able to construct sharp gradients near cities, and especially near middle-size cities.

Figure 9 compares CMAQ and OMI NO_2 VCDs using AK and DS methods together. Figure 9a shows a scatter-plot comparison between CMAQ and OMI NO_2 VCDs at U.S. Environmental Protection Agency Air Quality System (AQS) surface-monitoring site locations during September 2013. In this comparison, CMAQ NO_2 VCDs are much higher compared to OMI NO_2 VCDs, implying that the CMAQ simulation possibly overestimates NO_x emissions. Figure 9c compares OMI and CMAQ NO_2 VCD with AK information applied; estimated CMAQ NO_2 VCD is reduced, showing better agreement with OMI NO_2 VCD. Readers may notice that high CMAQ pixels are shifted to the left. On the other hand, applying the DS method to OMI shifts OMI pixels vertically (Figure 9b). Finally, in Figure 9d, both AK and DS methods are applied; this comparison shows the best agreement between OMI and CMAQ NO_2 VCD pixels. Its correlation coefficient R = 0.89 and the slope of line fit is 0.59. Clearly, the application of the AK and DS methods not only improved the satellite-model comparison in the high NO_2 concentration range but also significantly improved the comparison in the low NO_2 range (i.e., 0–10x10^{15} molecules/cm^2), implying that this method can help interpret NO_x emission in major and mid-size cities. We have conducted same analyses for all summer months in 2013 & 2014, and results are consistent.

The differences in spatial distributions between monthly averaged OMI and CMAQ NO_2 VCDs during September 2013 are shown in Figure 10. Positive values indicate that CMAQ NO_2 VCD is higher than OMI VCD, which should likely be interpreted as an overestimation of the NOx emission inventory used in the CMAQ modeling. The difference between the original OMI and CMAQ NO_2 VCDs show strong positive values over most urban locations (Figure 10a). Applying AK (Figure 10b) and DS (Figure 10c) reduce positive biases for major and middle-to-small cities, showing the best agreement when both AK and DS are included. NO_2 VCD is still overestimated over major cities—New York, Philadelphia, Detroit, and Chicago—as is expected from the continuous trend of NO_x emission reduction, but they are much weaker than in the original comparison. Slight overestimations over Baltimore, Washington D.C., Richmond, and Norfolk have almost disappeared We also notice broad underestimation of NO_2 VCD over Pennsylvania and West Virginia, which might be related to recent changes in this region, but detailed analysis is beyond the scope of this study. Another interesting feature is that there are spots of underestimation over small cities or local power plants; we therefore suspect the DS method slightly overweights urban emissions due to the lack of soil NOx emissions in the current modeling system.

5. Conclusion

This study reports that satellite footprint sizes might cause a considerable effect on the measurement of fine-scale urban NO_2 plumes. Comparing OMI NO_2 VCDs over North American urban cities to a 12-km CMAQ simulation from NOAA NAQFC, we found that OMI footprint-pixel sizes are too coarse to resolve urban plumes, resulting in possible underestimation (and overestimation of model NO_2 VCD) over the urban core and overestimation outside. In order to quantify this effect of resolution, we first conducted a perfect-model experiment. Pseudo-OMI data were constructed using fine-scale outputs of a model simulation, assuming that the fine-scale model output is a true measurement. To match the footprint coverage from real OMI pathways, we conducted conservative spatial regridding with the corresponding fine-scale model outputs to generate a set of pseudo OMI pixels.

When compared to the original data, the pseudo-OMI data clearly showed smoothed signals over urban locations, with 20–30 % underestimation over major cities and up to 100% bias over smaller urban areas. We then introduced conservative downscaling of OMI NO_2 VCD using spatial information from the fine-scale model to adjust the spatial distribution, also applying Averaging Kernel (AK) information to adjust the vertical structure. Four-way comparisons were conducted between OMI with and without downscaling and CMAQ with and without AK information. Results show that OMI and CMAQ NO_2 VCDs show the best agreement when both downscaling and AK methods are applied, with correlation coefficient R = 0.89.

These results should be considered when using satellite data in the evaluation of emission inventories and translating these data into decision-making around emission policy. Table 1 shows a summary of the comparisons between OMI and CMAQ NO_2 VCDs described in Figure 8 and Figure 9. When CMAQ without AK and OMI with DS are compared, the percentage difference is (6.43-3.61)/3.61*100 = 78%, implying that the current emission inventory likely overestimates NO_2 VCD. Comparing between OMI with DS and CMAQ without AK or between OMI without DS and CMAQ with AK still implies that the current emission inventory is possibly overestimating. However, when both vertical and spatial profiles are adjusted using the AK and DS methods, a slight underestimation is found, -7%, in modeled NO_2 VCD over AQS monitoring locations, implying that the current inventory possibly underestimates emissions. This may represent an important implication for how spatial information should be considered when investigating fine-scale phenomena such as urban NO_2 plumes.

Without question, satellite observations are very useful with their large coverage supplementing sparse surface-monitoring sites. Interpretation of satellite-based measurement, however, should be performed cautiously with consideration of the instrument's characteristics, especially when translating results into policy-making. We expect our current study to provide a reference for the uncertainty of satellite-based information regarding local or regional pollutants, especially until we have the measurement data at more enhanced resolution that will be provided by future satellites, such as Tropospheric Emissions: Monitoring of Pollution (TEMPO), Tropospheric Monitoring Instrument (TROPOMI), and Geostationary Environmental Monitoring Spectrometer (GEMS).

Appendix A: Conservative spatial regridding method

For the spatial regridding of satellite data, the IDL-based Geospatial Data Processor (IGDP) performs 'conservative spatial regridding' based the exact calculation of overlapped areas using the polygon clipping algorithm. This method differs from traditional interpolation method since it handles the geospatial data (e.g. satellite data) as "polygon with area" instead of "(dimensionless) pixels". This method reconstructs raw data pixels (e.g. satellite data) into target domain grid cells, by calculating fractional weighting of each overlapping portions between data pixels and domain grid cells. If the raw pixel data is in density units (e.g. concentration), the grid cell concentration can be calculated as a weighted average of data pixels and fractions (Figure 11).

$$f_{i,j} = \frac{Area(P_i \cap C_j)}{Area(C_j)}$$

$$C_j = \frac{\sum P_i \cdot f_{i,j}}{\sum f_{i,j}}$$

where i and j are indices of data pixel, P, and grid cells, C. $f_{i,j}$ is the overlapping fractions, and $\sum f_{i,j}$=1 if no missing pixels are involved in grid cell C_j.

If the satellite pixel data is in mass units, equations for the conservative remapping are slightly different. We need to calculate fractions of overlapped area to raw data pixel size, instead of grid cell size.

$$g_{i,j} = \frac{Area(P_i \cap C_j)}{Area(P_j)}$$

$$C_j = \sum P_i \cdot g_{i,j}$$

where $g_{i,j}$ is the fraction of overlapped area to the data pixel size.

Detailed information on the polygon clipping algorithms is described in Kim et al.,(2013).

Appendix B: IDL routines for downscaling method

Per the request of anonymous reviewer, we provide sample IDL routines of conservative spatial regridding and downscaling of OMI and CMAQ NO_2 VCDs in the supplementary materials with brief descriptions. Users will be able to download and test sample codes, and further modify the codes for their own interest.

Acknowledgements

The authors acknowledge the free use of tropospheric NO_2 column data from the OMI sensor from www.temis.nl. We gratefully appreciate Drs. Thomas Ryerson and Ilana Pollack for the P3 data from the CalNex campaign. The IGDP tool was developed by the support of University of Texas Air Quality Research Program (AQRP) and Texas Commission on Environmental Quality (TCEQ) (AQRP project 13-TN2). We are also grateful to two anonymous reviewers for their thorough comments and insightful suggestions.

References

Beirle, S., Platt, U., Wenig, M., & Wagner, T. (2004). Highly resolved global distribution of tropospheric NO_2 using GOME narrow swath mode data. *Atmospheric Chemistry and Physics Discussions*, *4*(2), 1665–1689. doi:10.5194/acpd-4-1665-2004

Beirle, Steffen, Boersma, K. F., Platt, U., Lawrence, M. G., & Wagner, T. (2011). Megacity emissions and lifetimes of nitrogen oxides probed from space. *Science (New York, N.Y.)*, *333*(6050), 1737–9. doi:10.1126/science.1207824

Boersma, K. F., Eskes, H. J., & Brinksma, E. J. (2004). Error analysis for tropospheric NO 2 retrieval from space. *Journal of Geophysical Research*, *109*(D4), D04311. doi:10.1029/2003JD003962

Boersma, K. F., Eskes, H. J., Veefkind, J. P., Brinksma, E. J., van der A, R. J., Sneep, M., … Bucsela, E. J. (2007). Near-real time retrieval of tropospheric NO2 from OMI. *Atmospheric Chemistry and Physics*, *7*(8), 2103–2118. doi:10.5194/acp-7-2103-2007

Bucsela, E. J., Perring, A. E., Cohen, R. C., Boersma, K. F., Celarier, E. A., Gleason, J. F., … Veefkind, J. P. (2008). Comparison of tropospheric NO 2 from in situ aircraft measurements with near-real-time and standard product data from OMI. *Journal of Geophysical Research*, *113*(D16), D16S31. doi:10.1029/2007JD008838

Chai, T., Kim, H.-C., Lee, P., Tong, D., Pan, L., Tang, Y., … Stajner, I. (2013). Evaluation of the United States National Air Quality Forecast Capability experimental real-time predictions in 2010 using Air Quality System ozone and NO_2 measurements. *Geoscientific Model Development*, *6*(5), 1831–1850. doi:10.5194/gmd-6-1831-2013

Chauhan, A., Inskip, H. M., Linaker, C. H., Smith, S., Schreiber, J., Johnston, S. L., & Holgate, S. T. (2003). Personal exposure to nitrogen dioxide (NO2) and the severity of virus-induced asthma in children. *The Lancet*, *361*(9373), 1939–1944. doi:10.1016/S0140-6736(03)13582-9

Cohan, D. S., Hu, Y., & Russell, A. G. (2006). Dependence of ozone sensitivity analysis on grid resolution. *Atmospheric Environment*, *40*(1), 126–135.

Eder, B., Kang, D., Mathur, R., Pleim, J., Yu, S., Otte, T., & Pouliot, G. (2009). A performance evaluation of the National Air Quality Forecast Capability for the summer of 2007☆. *Atmospheric Environment*, *43*(14), 2312–2320. doi:10.1016/j.atmosenv.2009.01.033

Eskes, H. J., & Boersma, K. F. (2003). Averaging kernels for DOAS total-column satellite retrievals. *Atmospheric Chemistry and Physics*, *3*(5), 1285–1291. doi:10.5194/acp-3-1285-2003

Gillani, N. V., & Pleim, J. E. (1996). Sub-grid-scale features of anthropogenic emissions of NOx and VOC in the context of regional eulerian models. *Atmospheric Environment*, *30*(12), 2043–2059. doi:10.1016/1352-2310(95)00201-4

Herron-Thorpe, F. L., Lamb, B. K., Mount, G. H., & Vaughan, J. K. (2010). Evaluation of a regional air quality forecast model for tropospheric NO2 columns using the OMI/Aura satellite tropospheric NO2 product. *Atmospheric Chemistry and Physics*, *10*(18), 8839–8854. doi:10.5194/acp-10-8839-2010

Heue, K., Wagner, T., Broccardo, S. P., Walter, D., Piketh, S. J., Ross, K. E., … Platt, U. (2008). Direct observation of two dimensional trace gas distributions with an airborne Imaging DOAS instrument. *Atmospheric Chemistry and Physics*, *8*(22), 6707–6717. doi:10.5194/acp-8-6707-2008

Hilboll, A., Richter, A., & Burrows, J. P. (2013). Long-term changes of tropospheric NO2 over megacities derived from multiple satellite instruments. *Atmospheric Chemistry and Physics*, *13*(8), 4145–4169. doi:10.5194/acp-13-4145-2013

Judd, L., Lefer, B., & Kim, H. C. (n.d.). Influences of environmental heterogeneity on OMI NO2 measurements and improvements using downscaling.

Kampa, M., & Castanas, E. (2008). Human health effects of air pollution. *Environmental pollution (Barking, Essex : 1987)*, *151*(2), 362–7. doi:10.1016/j.envpol.2007.06.012

Kim, H., Ngan, F., Lee, P., & Tong, D. (2013). *Development of IDL-based geospatial data processing framework for meteorology and air quality modeling*. Retrieved from http://aqrp.ceer.utexas.edu/projectinfoFY12_13%5C12-TN2%5C12-TN2 Final Report.pdf

Kim, S.-W., Heckel, a., Frost, G. J., Richter, a., Gleason, J., Burrows, J. P., … Trainer, M. (2009). NO 2 columns in the western United States observed from space and simulated by a regional chemistry model and their implications for NO x emissions. *Journal of Geophysical Research*, *114*(D11), D11301. doi:10.1029/2008JD011343

Kim, S.-W., Heckel, A., McKeen, S. a., Frost, G. J., Hsie, E.-Y., Trainer, M. K., … Grell, G. a. (2006). Satellite-observed U.S. power plant NO x emission reductions and their impact on air quality. *Geophysical Research Letters*, *33*(22), L22812. doi:10.1029/2006GL027749

Konovalov, I. B., Beekmann, M., Richter, a., & Burrows, J. P. (2006). Inverse modelling of the spatial distribution of NO_x emissions on a continental scale using satellite data. *Atmospheric Chemistry and Physics*, *6*(7), 1747–1770. doi:10.5194/acp-6-1747-2006

Lamsal, L. N., Martin, R. V., van Donkelaar, a., Steinbacher, M., Celarier, E. a., Bucsela, E., … Pinto, J. P. (2008). Ground-level nitrogen dioxide concentrations inferred from the satellite-borne Ozone Monitoring Instrument. *Journal of Geophysical Research*, *113*(D16), 16308. doi:10.1029/2007JD009235

Levelt, P., van den Oord, G. H. J., Dobber, M. R., Malkki, A., Stammes, P., Lundell, J. O. V., & Saari, H. (2006). The ozone monitoring instrument. *IEEE Transactions on Geoscience and Remote Sensing*, *44*(5), 1093–1101. doi:10.1109/TGRS.2006.872333

Liang, J., & Jacobson, M. Z. (2000). Effects of subgrid segregation on ozone production efficiency in a chemical model. *Atmospheric Environment*, *34*(18), 2975–2982. doi:10.1016/S1352-2310(99)00520-8

Martin, R. V., Jacob, D. J., Chance, K., Kurosu, T. P., Palmer, P. I., & Evans, M. J. (2003). Global inventory of nitrogen oxide emissions constrained by space-based observations of NO 2 columns. *Journal of Geophysical Research*, *108*(D17), 4537. doi:10.1029/2003JD003453

Napelenok, S. L., Pinder, R. W., Gilliland, a. B., & Martin, R. V. (2008). A method for evaluating spatially-resolved NO_x emissions using Kalman filter inversion, direct sensitivities, and space-based NO_2 observations. *Atmospheric Chemistry and Physics Discussions*, *8*(2), 6469–6499. doi:10.5194/acpd-8-6469-2008

Pan, L., Tong, D., Lee, P., Kim, H.-C., & Chai, T. (2014). Assessment of NOx and O3 forecasting performances in the U.S. National Air Quality Forecasting Capability before and after the 2012 major emissions updates. *Atmospheric Environment*, *95*(x), 610–619. doi:10.1016/j.atmosenv.2014.06.020

Richter, A., Burrows, J. P., Nüss, H., Granier, C., & Niemeier, U. (2005). Increase in tropospheric nitrogen dioxide over China observed from space. *Nature*, *437*(7055), 129–32. doi:10.1038/nature04092

Rijnders, E., Janssen, N. A. H., van Vliet, P. H. N., & Brunekreef, B. (2001). Personal and Outdoor Nitrogen Dioxide Concentrations in Relation to Degree of Urbanization and Traffic Density. *Environmental Health Perspectives*, *109*(2), 411. doi:10.2307/3434789

Ross, Z., English, P. B., Scalf, R., Gunier, R., Smorodinsky, S., Wall, S., & Jerrett, M. (2006). Nitrogen dioxide prediction in Southern California using land use regression modeling: potential for environmental health analyses. *Journal of exposure science & environmental epidemiology*, *16*(2), 106–14. doi:10.1038/sj.jea.7500442

Ryerson, T. B., Andrews, a. E., Angevine, W. M., Bates, T. S., Brock, C. a., Cairns, B., … Wofsy, S. C. (2013). The 2010 California Research at the Nexus of Air Quality and Climate Change (CalNex) field study. *Journal of Geophysical Research: Atmospheres*, *118*(11), 5830–5866. doi:10.1002/jgrd.50331

Sillman, S., Logan, J. A., & Wofsy, S. C. (1990). The sensitivity of ozone to nitrogen oxides and hydrocarbons in regional ozone episodes. *Journal of Geophysical Research*, *95*(D2), 1837–1851. doi:10.1029/JD095iD02p01837

Studinicka, M., Hackl, E., Pischinger, J., Fangmeyer, C., Haschke, N., K¨hr, J., … Frischer, T. (1997). Traffic-related NO2 and the prevalence of asthma and respiratory symptoms in seven year olds. *European Respiratory Journal*, *10*(10), 2275–2278. doi:10.1183/09031936.97.10102275

Valin, L. C., Russell, a. R., Hudman, R. C., & Cohen, R. C. (2011). Effects of model resolution on the interpretation of satellite NO2 observations. *Atmospheric Chemistry and Physics*, *11*(22), 11647–11655. doi:10.5194/acp-11-11647-2011

Van der A, R. J., Eskes, H. J., Boersma, K. F., van Noije, T. P. C., Van Roozendael, M., De Smedt, I., … Meijer, E. W. (2008). Trends, seasonal variability and dominant NO x source derived from a ten year record of NO 2 measured from space. *Journal of Geophysical Research*, *113*(D4), D04302. doi:10.1029/2007JD009021

Van der A, R. J., Peters, D. H. M. U., Eskes, H., Boersma, K. F., Van Roozendael, M., De Smedt, I., & Kelder, H. M. (2006). Detection of the trend and seasonal variation in tropospheric NO 2 over China. *Journal of Geophysical Research*, *111*(D12), D12317. doi:10.1029/2005JD006594

	OMI/xDS (mean = 3.61)	OMI/DS (mean = 5.00)
CMAQ/xAK (mean = 6.43)	S = 0.28 R = 0.79 (6.43-3.61)/3.61*100 = 78.1 %	S = 0.45 R = 0.87 (6.43-5)/5*100 = 28.6 %
CMAQ/AK (mean = 4.65)	S = 0.39 R = 0.87 (4.65-3.61)/3.61*100 = 28.8%	S = 0.59 R = 0.89 (4.65-5)/5*100 = -7.0 %

Table 1. Comparison of OMI and CMAQ NO_2 VCD monthly averages (Sep. 2013) at AQS sites.

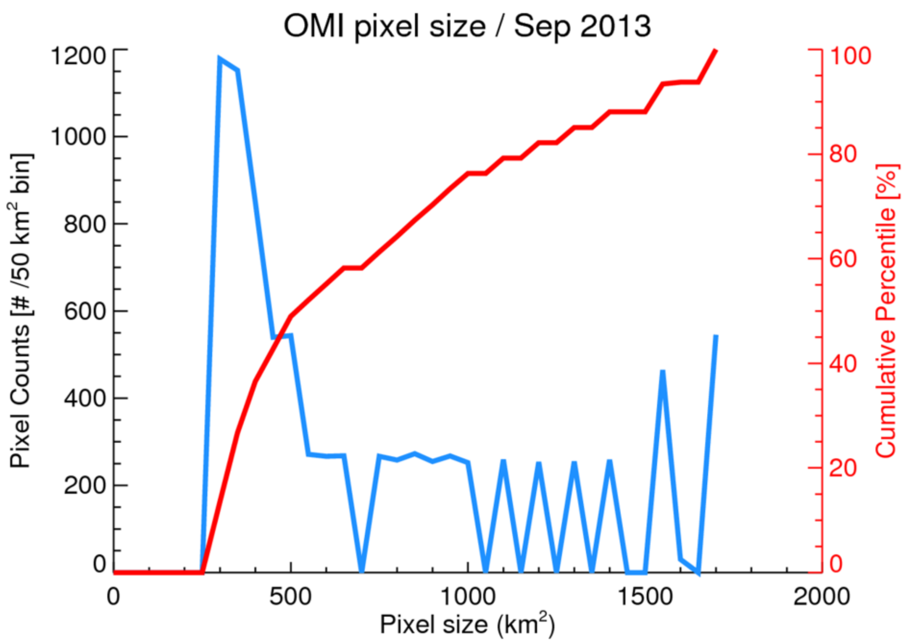

Figure 1. Size distribution of OMI pixel footprint (blue) and its cumulative percentile (red) during September 2013.

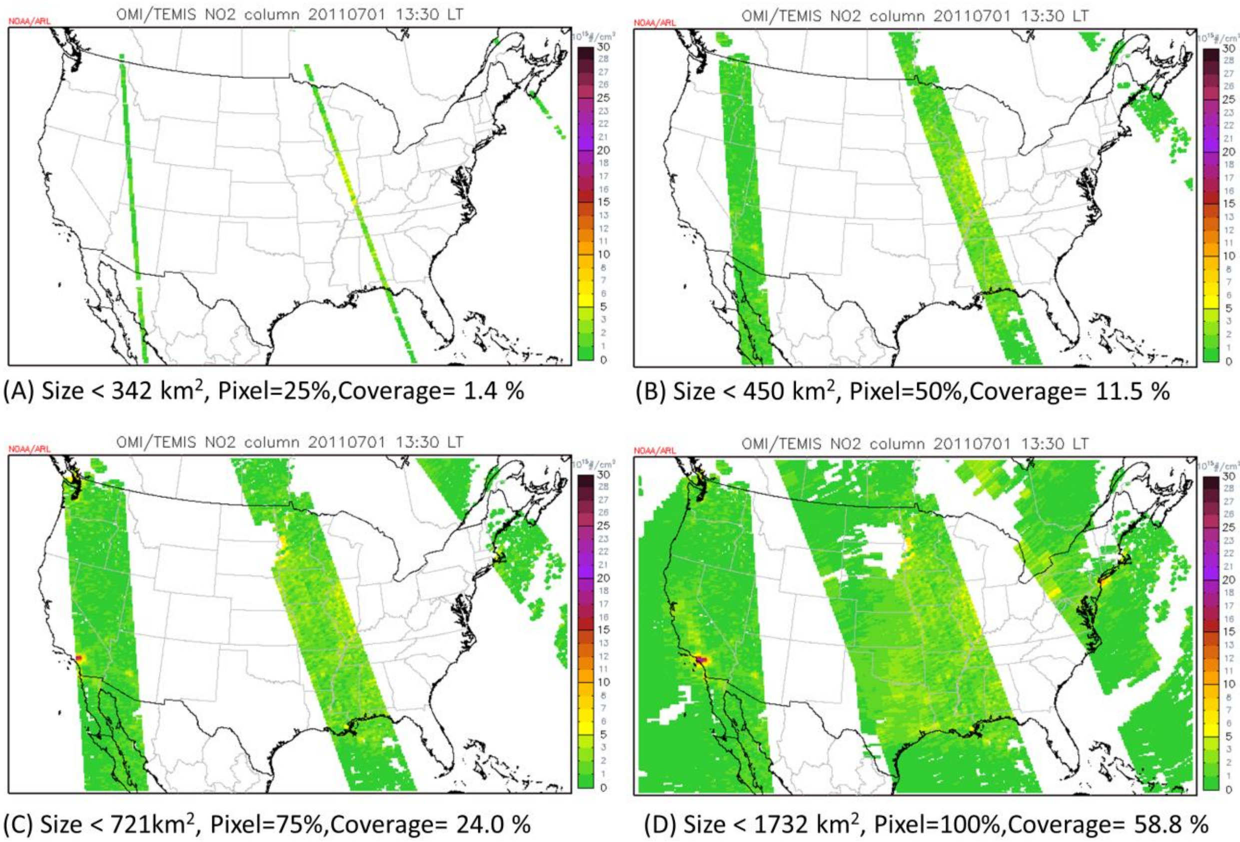

Figure 2. Comparison of OMI footprint-pixel size and actual coverage using (a) 25%, (b) 50%, (c) 75%, and (d) 100% of available pixels on July 1, 2011.

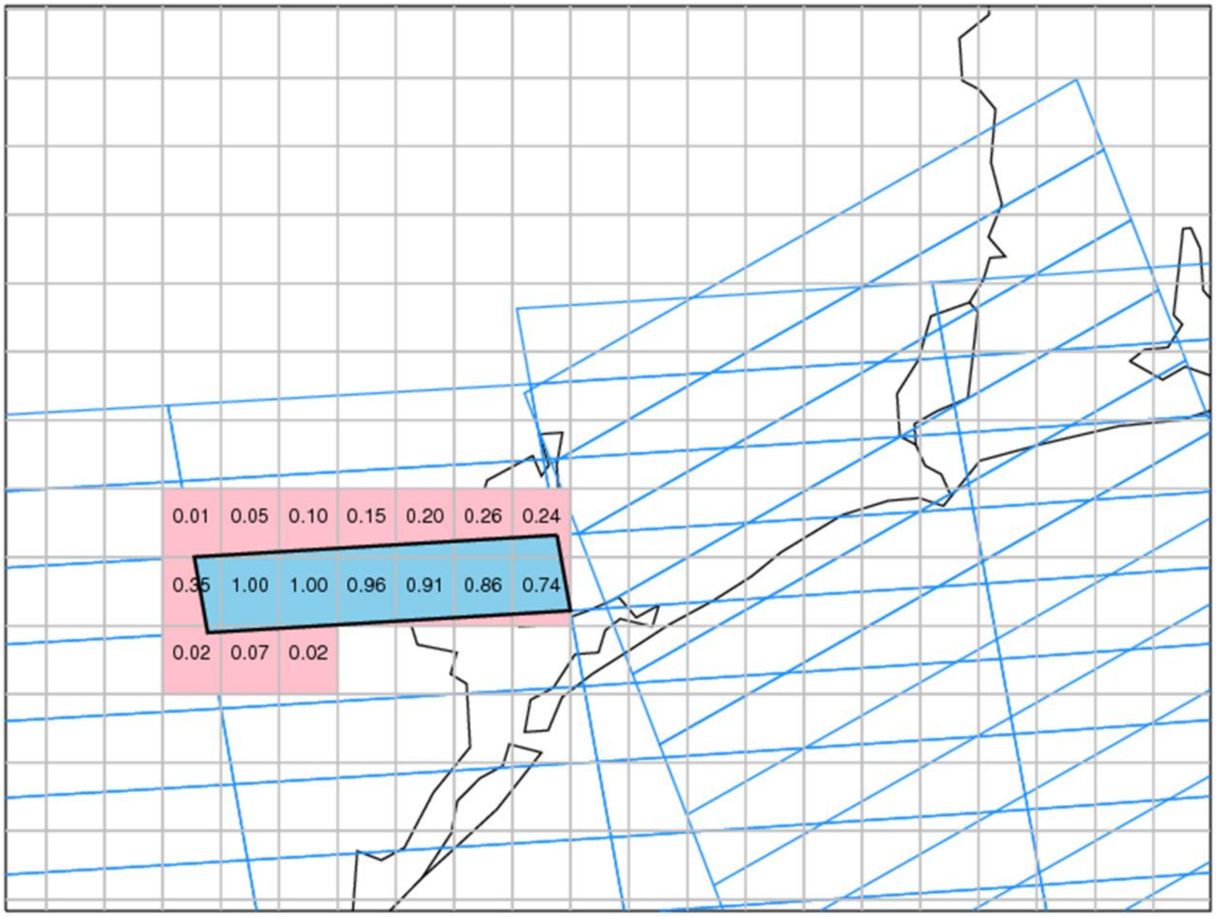

Figure 3. Calculation of pseudo-OMI (pOMI) data. Blue boxes are actual OMI pixel footprints and the gray cells are 12-km grid cells. Fraction of cells overlapped by an OMI pixel are shown, and pOMI (sky blue) data are estimated by a weighted average of the corresponding grid cells (pink).

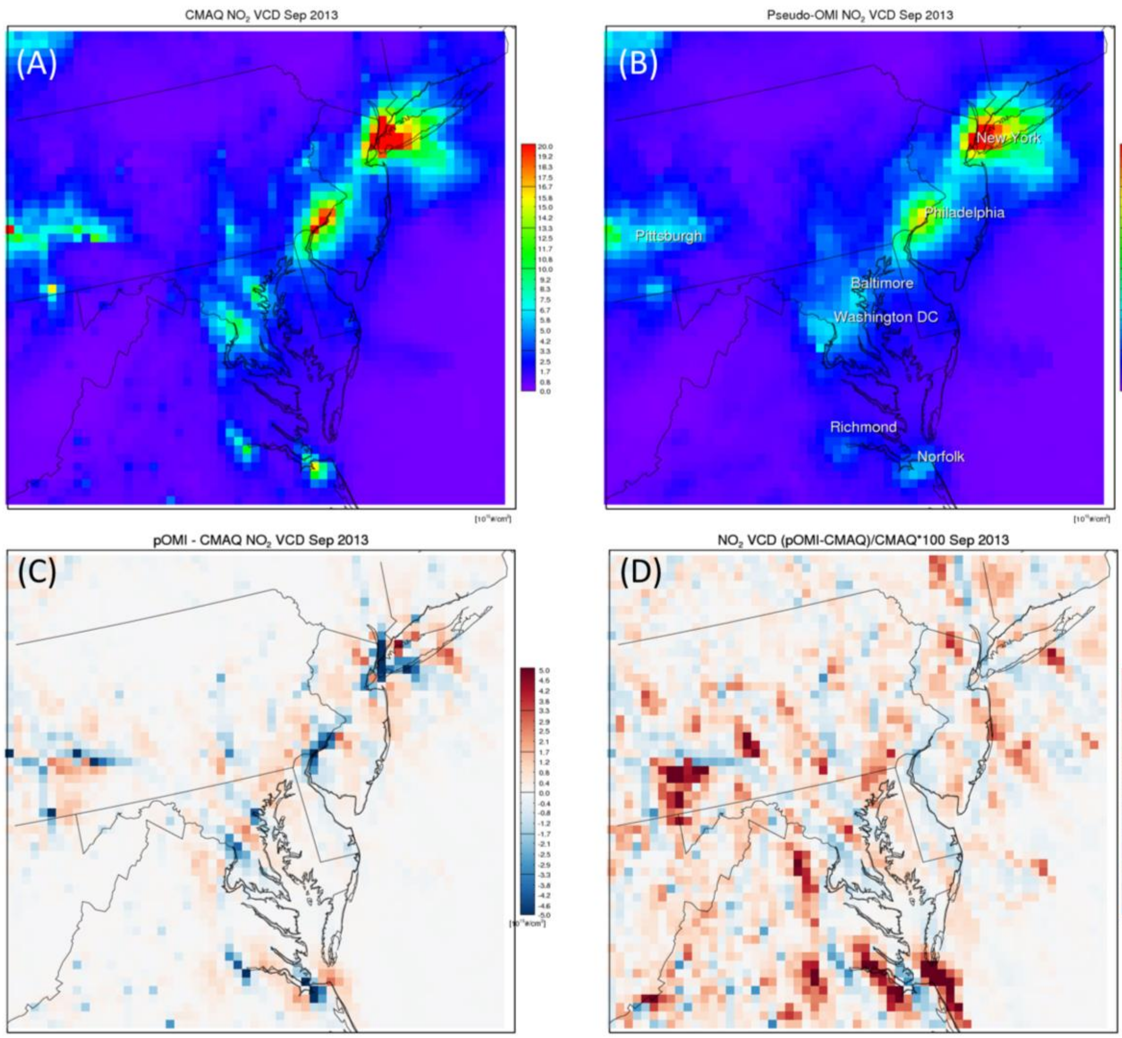

Figure 4. Monthly mean distribution of (a) CMAQ, (b) pOMI NO_2, (c) difference (pOMI-CMAQ), and (d) percentage difference (pOMI-CMAQ)/CMAQ*100 during September 2013.

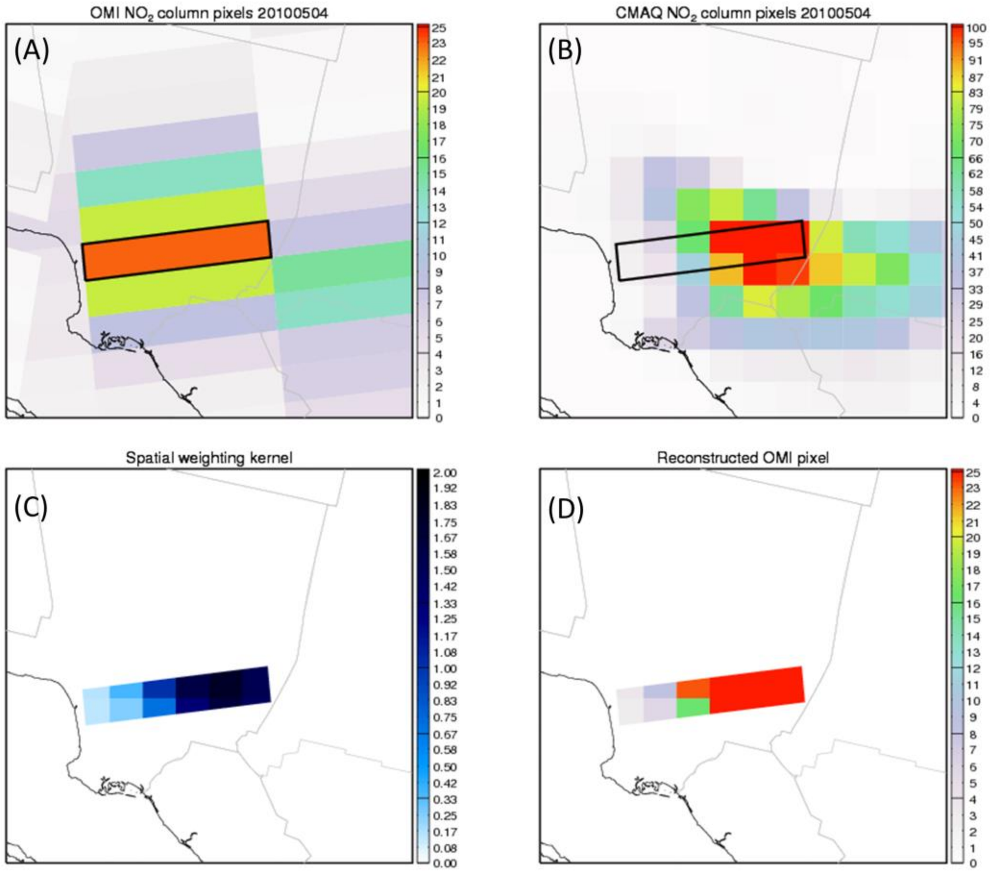

Figure 5. Example of downscaling method. (a) Original OMI NO_2 VCD, (b) 12-km CMAQ NO_2 VCD, (c) spatial weighting kernel, and (d) adjusted OMI NO_2 VCD using spatial weighting kernel.

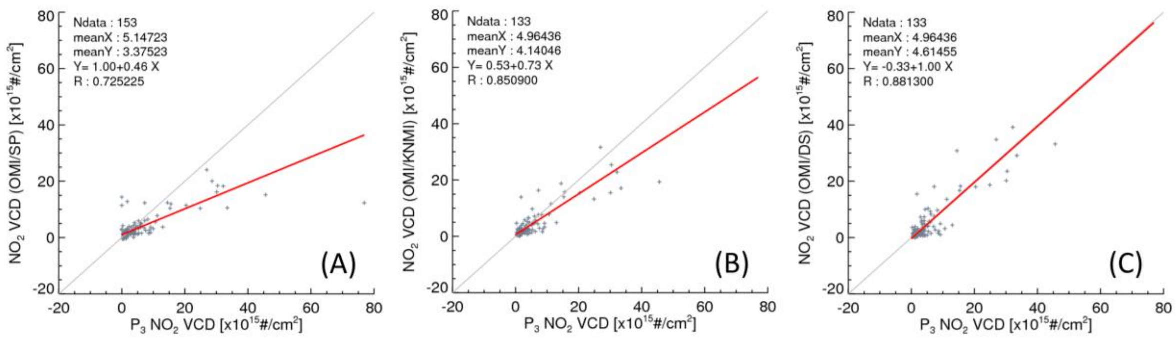

Figure 6. Scatter plots of P3 and OMI NO_2 VCD for (a) OMI standard products, (b) OMI KNMI, and (c) OMI KNMI with downscaling for May 4, 7 & 16,2010.

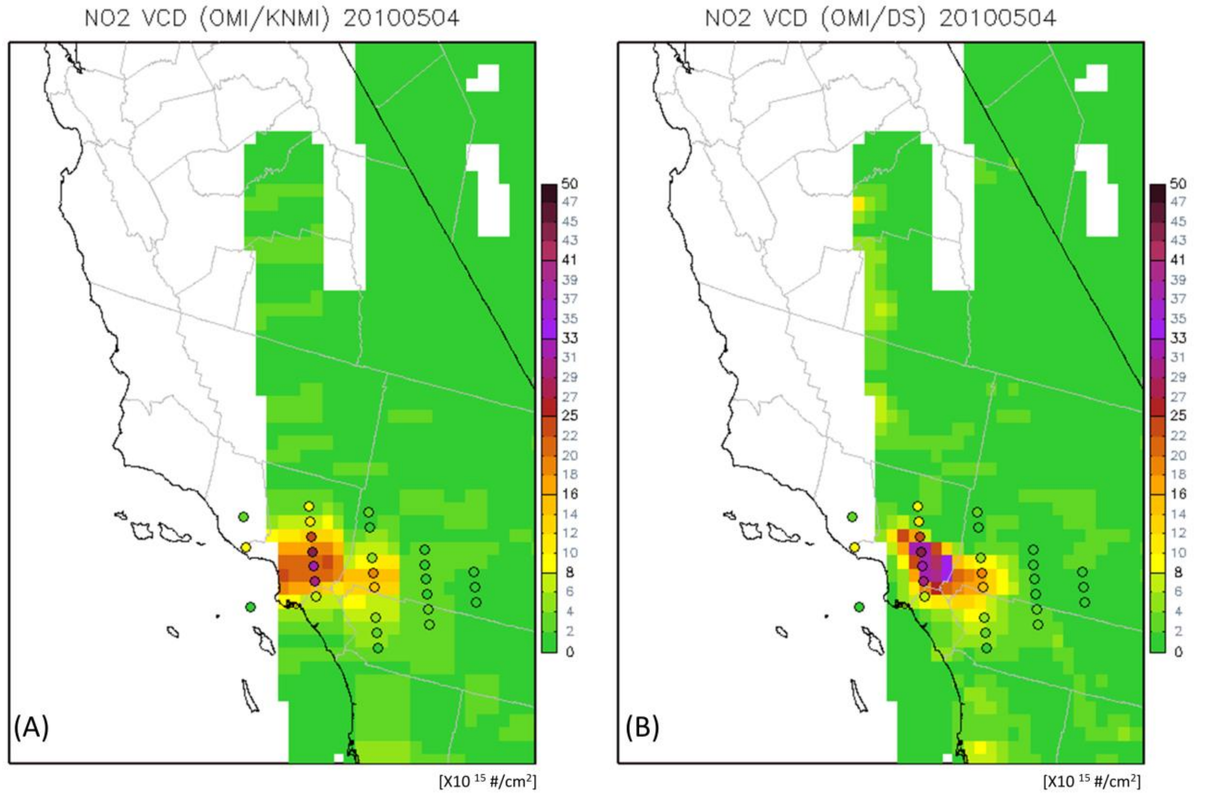

Figure 7 Spatial distribution of P3 NO_2 VCDs (circles) and OMI NO_2 VCDs for original KNMI product (A), and downscaled OMI (B) for 4 May 2010.

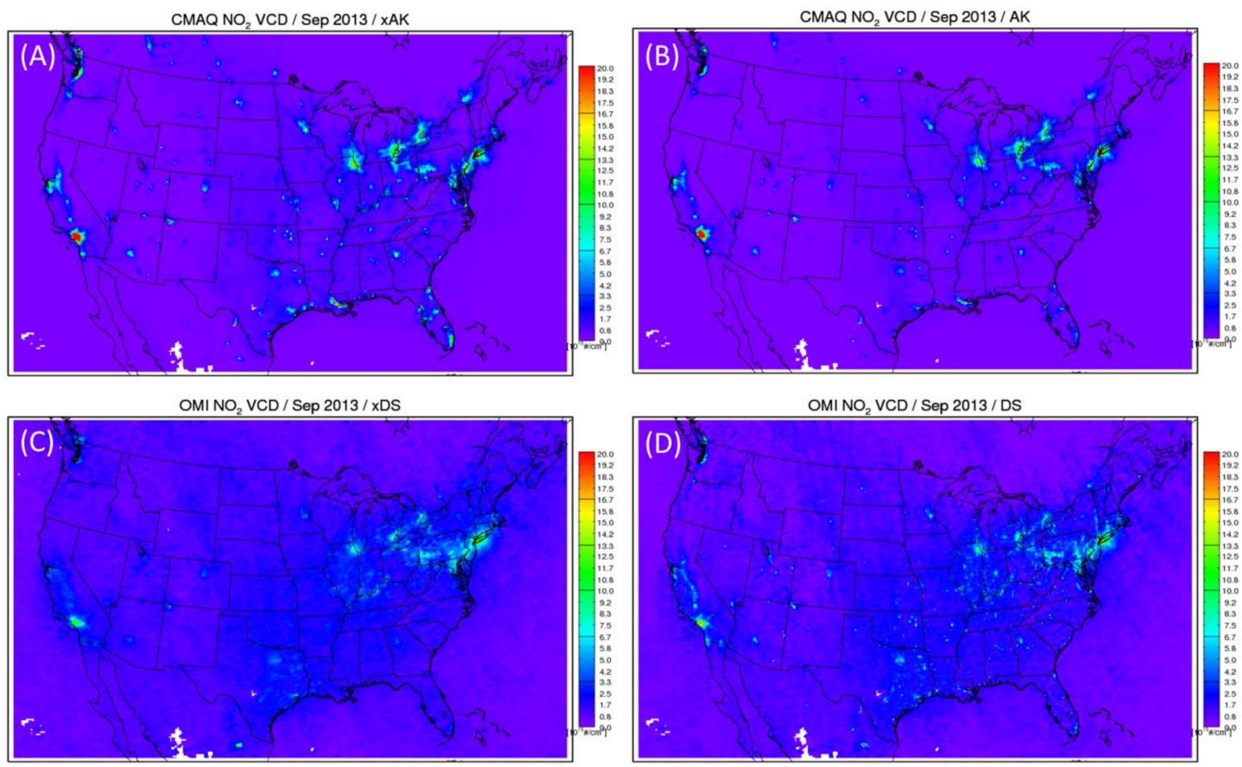

Figure 8. Spatial distributions of (a) CMAQ NO_2 VCD without AK and (b) with AK; (c) OMI NO_2 VCD without downscaling and (d) with downscaling during September 2013.

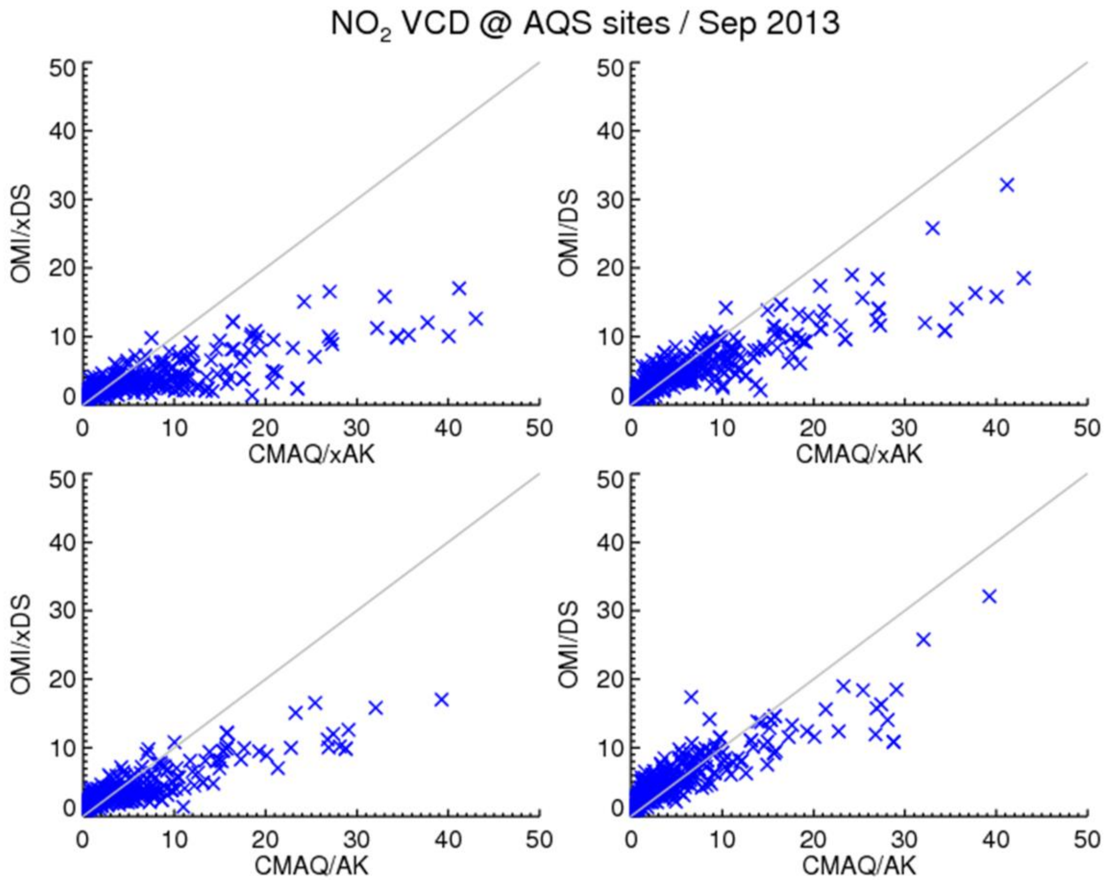

Figure 9. Comparison of OMI and CMAQ NO_2 VCD for (a) OMI and CMAQ with AK, (b) downscaled OMI and CMAQ with AK, (c) OMI and CMAQ with AK, and (d) downscaled OMI and CMAQ with AK during September 2013.

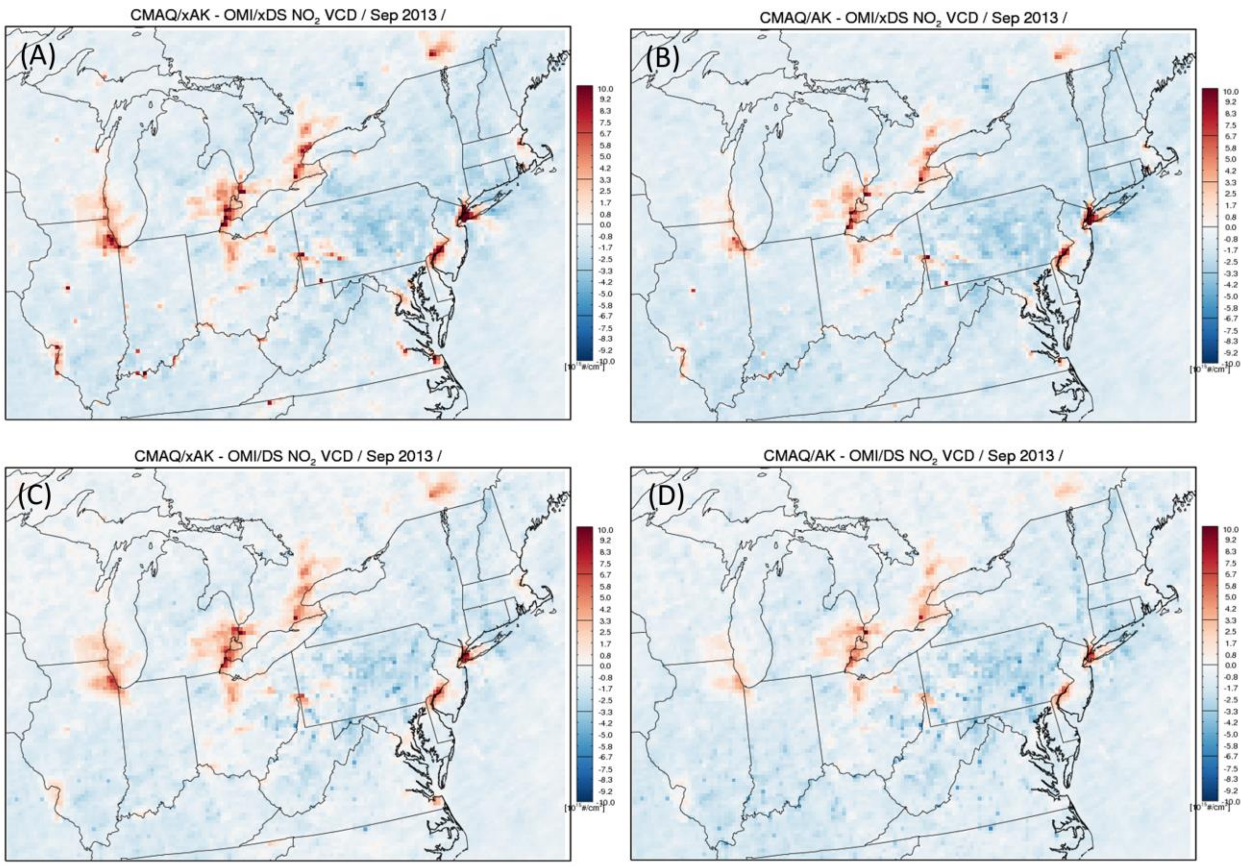

Figure 10. Comparisons of OMI and CMAQ NO_2 VCD spatial distributions in the northeast U.S. region during September 2013.

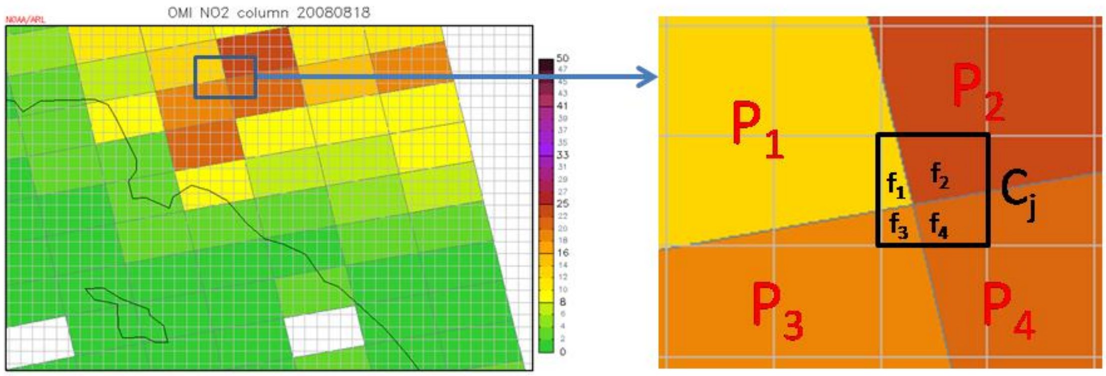

Figure 11 Example of "Conservative spatial regridding" method using variable-pixel linear reconstruction algorithm.